PERGAMON

International Journal of Mechanical Sciences 44 (2002) 489–507

International Journal of MECHANICAL SCIENCES

www.elsevier.com/locate/ijmecsci

Forging simulation of sintered powder compacts under various frictional conditions

Cheng-Chao Huang, Jung-Ho Cheng*

Department of Mechanical Engineering, National Taiwan University No. 1, Sec. 4, Roosevelt Road, Taipei 10617, Taiwan

Received 14 March 2001; received in revised form 27 November 2001

Abstract

This research is to investigate the deformation characteristics of sintered compacts and the evolution of voids in the forging process under different frictional conditions. The Gurson–Tvergaard yield criterion was used to describe the plastic behaviour of porous materials, while the material parameters were empirically determined.

Experiments and finite element analysis were conducted to examine the processes. The material properties of sintered preforms were ascertained from both the uni-axial tension and compression tests. The finite element models were verified with the upsetting experiments under different frictional conditions. A simulation of forging the gear blank under various contact situations was performed as well. Studies show that voids lead to the degradation of the strength of the sintered materials. Friction at contact interfaces contributes to the non-uniformity of deformation and the density variation in the workpiece after large deformation.

Keywords: Powder forging; Porous materials; Plasticity; Yield criteria; Porosity; Finite element method (FEM)

1. Introduction

Powder forging (P/F) combines powder metallurgy (P/M) and forging technologies and thus possesses the advantages of both processes that result in stronger yet versatile products with complicated geometry and arbitrary alloy compositions. Preforms are prepared in various steps that involve powder mixing, compacting, and sintering. The exact shape is obtained from a final forging procedure. This method results in fewer dies, less material waste, and lower tooling costs. However,

* Corresponding author. Fax: +886-2-2363-1755.

E-mail addresses: r1852206@w3.me.ntu.edu.tw (C.-C. Huang), jhcheng@w3.me.ntu.edu.tw (J.-H. Cheng).

0020-7403/02/$ - see front matter
PII: S0020-7403(01)00107-2

Nomenclature

Φ	potential function
$\boldsymbol{\sigma}$	macroscopic Cauchy stress tensor
$\mathbf{S}$	deviatoric part of the Cauchy stress tensor
$\mathbf{I}$	identity matrix
σ_h	hydrostatic stress
$\bar{\sigma}$	von Mises effective stress
σ_y	flow stress of a fully dense matrix
$\sigma_{first\ yield}$	first yield stress of the porous materials or a fully dense matrix
τ_{eq}	equivalent frictional stress
$\tau_{1,2}$	shear stress components
τ_{crit}	critical stress
p	contact pressure
μ	coefficient of friction
$\bar{\varepsilon}_m^p$	effective plastic strain of a fully dense matrix
$\dot{\bar{\varepsilon}}_m^p$	effective plastic flow of a fully dense matrix
$\dot{\boldsymbol{\varepsilon}}^p$	plastic flow of the materials
$\dot{\lambda}$	nonnegative plastic flow multiplier
f	void volume fraction (porosity)
$\dot{f}$	total change of void volume fraction
$\dot{f}_g$	change of growth of existing voids
$\dot{f}_n$	change of nucleation of new voids
$q_{1,2,3}$	material parameters
q_{j_s}	temporarily updated value of the material parameters ($j = 1$–3)
q_{j_p}	previous value of the material parameters ($j = 1$–3)
N	total number of data for the porous materials at the first yielding state
$(\boldsymbol{\sigma}_i, f_i)$	one set data of the porous materials at the first yielding state ($i = 1$–N)
k	coefficient in the plastic equation of a fully dense matrix
n	strain hardening exponent
E	Young's modulus
v	Poisson's ratio

voids in sintered compacts bear a detrimental effect on the mechanical properties, and the variation of density may occur in workpieces after large deformation.

After over four decades of development, the elastic–plastic problems of sintered materials have been widely studied. The expanding literature of relevant subjects is overwhelming. A yield criterion for porous media was proposed and modified by Gurson [1], Tvergaard [2], Richmond and Smelser [3], and Goya et al. [4]. The plastic behaviour of porous metals were examined by Kuhn and Downey [5], Green [6], Oyane et al. [7], Shima and Oyane [8], Doraivelu et al. [9], Hwang and

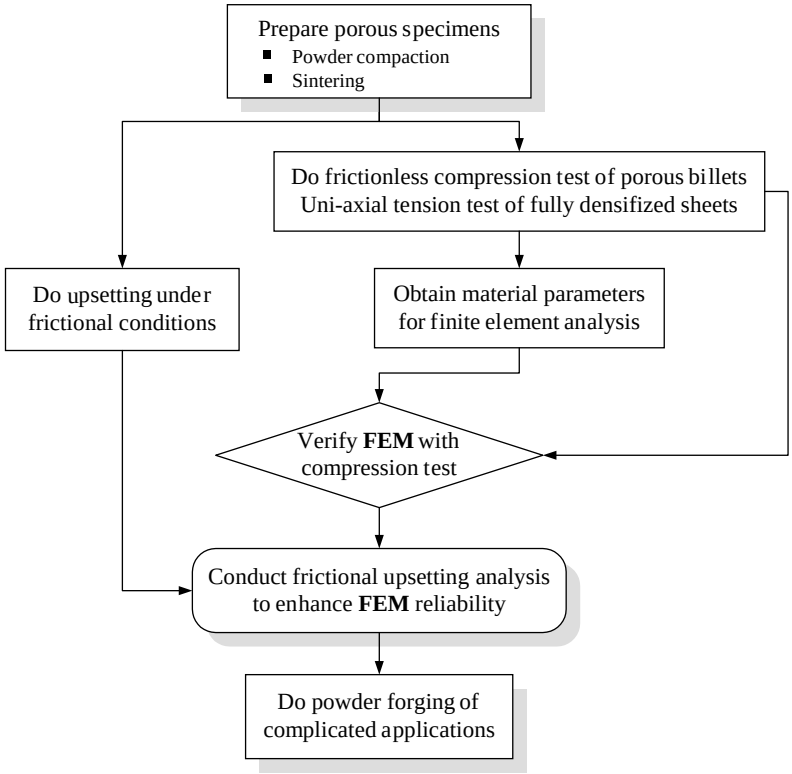

Fig. 1. The flow chart of this research.

Kobayashi [10], Mear [11], Lee and Kim [12], Lee and Mear [13], Nagaki et al. [14], Dias and Schaeffer [15], and Akisanya [16] as well.

The plastic flow and the density distribution in porous materials during deformation were presented by Mear and Durban [17], Bruhns and Sluzalec [18], Wang and Karabin [19], and Han et al. [20]. On the other hand, the deformation characteristics and fracture of iron compacts with different initial porosity were investigated by Spitzig et al. [21], Biner and Spitzig [22], and Spitzig [23]. The frictional conditions in the working process were analysed by Hartley et al. [24], Jha and Kumar [25], and Mamalis et al. [26]. In the consideration of the hot working operation, the effects of temperature on the processing parameters and the deformation behaviour of porous metals were studied by Bockstiegel and Olsen [27], Kim and Cho [28], and Han et al. [29].

Despite the close scrutiny of the plastic behaviour of porous metals, the evolution of voids and the effects of frictional conditions still elude sweeping generalization. The main purpose of this study, therefore, is to investigate the deformation characteristics of sintered compacts and the evolution of voids in the forging process under different frictional conditions (Fig. 1). This study started from preparing the porous preforms through the P/M steps with the metal powder. The material properties of sintered compacts were ascertained from the simple tension and compression tests. Then, the finite element models were established and verified with the upsetting experiments under different frictional

conditions. At the last step, the simulation of forging a gear blank under various contact situations was performed as well.

2. Theoretical review

2.1. Yield criteria and void evolution

The plastic theories of metals have been widely examined. The von Mises yield criterion, which is based on the shape distortion energy for fully dense media, is presented in the following equation:

$$\boldsymbol{\Phi}(\boldsymbol{\sigma}) = \bar{\sigma} - \sigma_y = 0, \tag{1}$$

where σ_y is the flow stress of fully dense media,

$$\bar{\sigma} = \sqrt{\tfrac{3}{2}\mathbf{S} : \boldsymbol{S}} \tag{2}$$

is the von Mises effective stress,

$$\mathbf{S} = \boldsymbol{\sigma} - \sigma_h \mathbf{I} \tag{3}$$

is the deviatoric part of the macroscopic Cauchy stress tensor $\boldsymbol{\sigma}$,

$$\sigma_h = \tfrac{1}{3}\boldsymbol{\sigma} : \mathbf{I} \tag{4}$$

is the hydrostatic stress, and $\mathbf{I}$ is the identity matrix.

For the yield function of porous media, Gurson [1] proposed a formula based on a rigid-plastic upper bound solution for the symmetric deformations of spherical voids in a deforming solid. This criterion combines the effects of both the deviatoric part and the hydrostatic component, and is represented as follows:

$$\boldsymbol{\Phi}(\boldsymbol{\sigma}, f) = \left(\frac{\bar{\sigma}}{\sigma_y}\right)^2 + 2q_1 f \cosh\left(\frac{3q_2\sigma_h}{2\sigma_y}\right) - (1 + q_3 f^2) = 0, \tag{5}$$

where f is the void volume fraction, σ_y is the flow stress of a matrix, and q_1, q_2, and q_3 are the material parameters. Originally it was demonstrated that $q_1 = q_2 = q_3 = 1$ in Eq. (5). Then, the scalar parameters with $q_1 = 1.5, q_2 = 1$, and $q_3 = q_1^2$ were introduced by Tvergaard [2] to make the predictions of the Gurson model agree with numerical studies. With the value of porosity being given as zero, $f = 0$, the Gurson–Tvergaard criterion can be simplified to the von Mises formula for a fully dense matrix.

On the other hand, the plastic flow of the materials is assumed to be normal to the yield surface

$$\dot{\boldsymbol{\varepsilon}}^p = \dot{\lambda}\frac{\partial \boldsymbol{\Phi}}{\partial \boldsymbol{\sigma}}, \tag{6}$$

where $\dot{\lambda}$ is the nonnegative plastic flow multiplier.

The constitutive equation of a matrix is described as $\bar{\sigma} = \bar{\sigma}(\bar{\varepsilon}_m^p)$, where $\bar{\varepsilon}_m^p$ is the effective plastic strain of the matrix. The evolution of the effective plastic strain in the matrix is obtained from the following effective plastic work expression:

$$(1 - f)\sigma_y \dot{\bar{\varepsilon}}_m^p = \boldsymbol{\sigma} : \dot{\boldsymbol{\varepsilon}}^p. \tag{7}$$

Observing the deformation mechanisms in porous metals, the total change of the void volume fraction during deformation arises partly from the growth of existing voids and partly from the nucleation of new voids, stated as

$$\dot{f} = \dot{f}_g + \dot{f}_n, \tag{8}$$

where $\dot{f}_g$ is the growth rate of existing voids and $\dot{f}_n$ is the change of the nucleation of new voids. The growth of existing voids is based on the law of conservation of mass and is expressed as

$$\dot{f}_g = (1 - f)\dot{\boldsymbol{\varepsilon}}^p : \mathbf{I}. \tag{9}$$

On the other hand, the nucleation of new voids stems from the grain boundaries or decohesion of the particle–matrix interface in the tensile stress state. Void nucleation at a material point, therefore, will not be considered in the compressive stress state. The mechanisms of void growth and nucleation during plastic deformation were sequentially reviewed by Goods and Brown [30], Chu and Needleman [31], Hom and McMeeking [32], and Lee and Zhang [33].

2.2. Frictional conditions

Generally, the frictional conditions at the contact interfaces of the workpiece and the die in bulk metal forming are essentially complex. In this research, the globally equivalent frictional forces were approximated to describe the contact situations. A standard Coulomb friction model with an additional limit on the allowable shear stress was used. It is assumed that no relative motion occurs if the equivalent frictional stress,

$$\tau_{eq} = \sqrt{\tau_1^2 + \tau_2^2} \tag{10}$$

is less than the critical stress, τ_{crit}, which is proportional to the contact pressure, p, in the form below

$$\tau_{crit} = \mu p, \tag{11}$$

where μ is the coefficient of friction, based on trial and error in the finite element simulation for matching the practical results. In addition, τ_1 and τ_2 in Eq. (10) are the components of the shear stress.

2.3. Material parameters

The Gurson–Tvergaard yield criterion was adopted to describe the plastic behaviour of porous materials in this study. Emphatically, the scalar parameters, q_1, q_2, and q_3, were empirically determined. The computing loop for fitting the parameters is illustrated in Fig. 2. A least-squares method was used to formulate the objective function, which is stated as

$$\mathrm{Fun}(q_j) = \sum_{i=1}^{N} [\boldsymbol{\Phi}(\boldsymbol{\sigma}_i, f_i)]^2, \quad j = 1\text{–}3, \tag{12}$$

where $\boldsymbol{\sigma}_i$ and f_i are the values of one set of the data, and q_j is the scalar parameter from q_1 to q_3. The total amount of the data sets, N, is equal to 45. The initial value of three scalar parameters

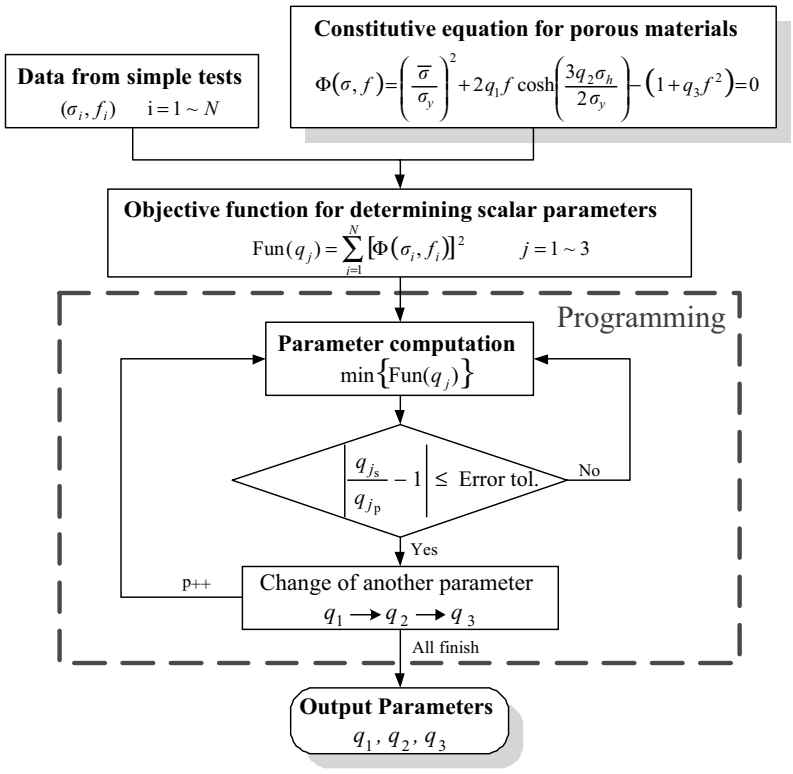

Fig. 2. The computing loop for fitting the material parameters from the experimental data.

was given as 1.0 in the program. This computation recognizes the dependence of the ability of the loop convergence upon the level of the error tolerance criterion,

$$\left|\frac{q_{j_s}}{q_{j_p}}-1\right| \leqslant \text{Error tol.}, \quad j=1\text{–}3, \tag{13}$$

where q_{j_s} is the temporarily updated value computed in the current loop for substituting the previous value, q_{j_p}, if the criterion is satisfied. The error tolerance is defined from the user. After the process of a convergent calculation, the undetermined parameter in the objective function was transferred from one to another consecutively until the fitting procedures for all parameters were finished. At the final stage, these optimum parameters were output, and they were quoted in the finite element model.

3. Experimental procedures

3.1. Specimens preparation

The porous specimens used in the experiments were prepared from the water-atomized pure iron powder. The constituents and the distributions of particle size are demonstrated in Table 1. The

Table 1
The powder constituent and the particle size distribution

The properties of water-atomized iron powders (KIP 301A)				
Chemical analysis		Screen analysis		
Constituent	%	Mesh	Particle size (μm)	%
Fe	Bal.	+60	+250	—
M. Fe	—	+80	+180	⩽ 2
C	⩽ 0.01	+100	+150	⩽ 15
Si	⩽ 0.05	+150	+106	10–30
Mn	0.10–0.25	+200	+75	10–40
P	⩽ 0.025	+250	+63	⩽ 25
S	⩽ 0.025	+325	+45	5–30
O	⩽ 0.25	−325	−45	10–30

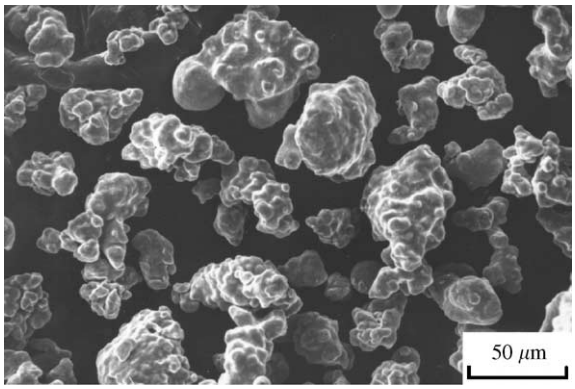

Fig. 3. The scanning electron micrograph of the water-atomized iron powder.

irregular particle shape (Fig. 3), which increases the mechanical locking between powders, can enhance the green strength of the compacts and reduce the volume contraction during the sintering step. Various compacting pressures and the floating die method were utilized to prepare the billets with different green densities. The compacted billet is 12.5 mm in diameter, and the height is controlled by weight to make the aspect ratio (the height-to-diameter ratio) < 1.5 to prevent the specimens from buckling in the compression tests.

It is a well-known fact that the die compaction of powders results in the anisotropic compacts, which may cause the non-uniform concentration of volume and the shape distortion of the preforms in the sintering step. Furthermore, the anisotropic distributions of voids in the workpieces yield the non-uniform deformation and reduce the forging capability. In this study, the lubricant that dissolves 100 g of zinc stearate in 1 l of acetone was used to improve the lubricating conditions in the compacting step.

All the compacts were sintered in dry hydrogen at 1200°C for 1 h and then cooled down in the furnace to room temperature. In order to determine the mechanical properties of the matrix, some specimens were fully densified by rolling. Since the microstructure plays a significant role on the

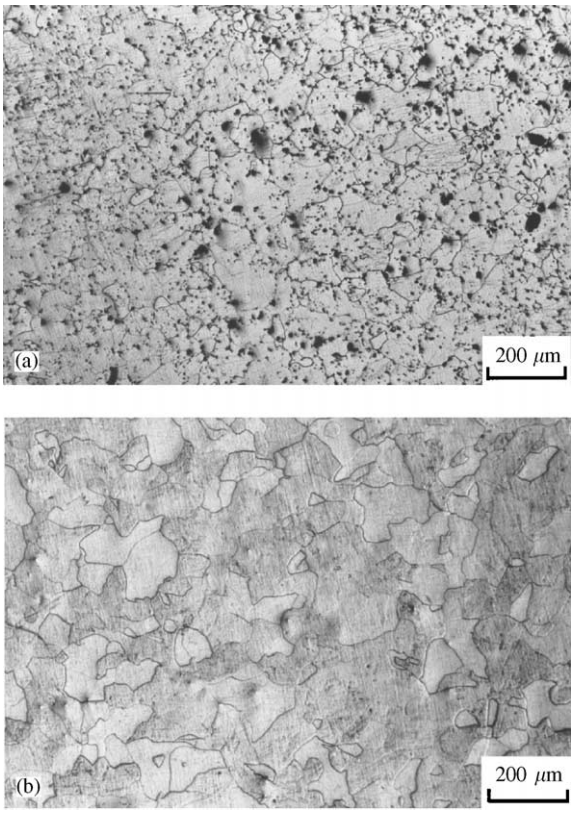

Fig. 4. The optical micrograph of: (a) the porous pure iron; and (b) the fully dense matrix.

plastic behaviour, the process of recrystallization in dry hydrogen at 600°C for 10 min was needed to dispel the hardening induced in the rolling process. The microstructure of the porous compacts and the fully dense matrix are demonstrated in Fig. 4, where the grain size in the matrix after recrystallization is similar to that in the porous metals.

3.2. Simple tension and frictionless compression tests for material parameters

The material properties of the sintered preforms were ascertained from both the uni-axial tension and compression tests. In the tension tests, the specimens were made of the fully densified sheets. They measure 50 mm in gauge length, 12.5 mm in width, and 2–3 mm in thickness. The material constants, Young's modulus, Poisson's ratio, the first yield stress, and the plastic behaviour of the matrix were obtained. A strain gauge and an extensometer were utilized to monitor the deformation in the axial and transverse directions. The tensile true stress-strain curve of the fully dense matrix is demonstrated in Fig. 5, where the first yield stress is found to be 126 MPa. The plastic behaviour of the matrix reveals a power-law relation, $\bar{\sigma} = k(\bar{\varepsilon}_m^p)^n$, where the coefficient k is fitted at the value of 543.63 MPa and the strain hardening exponent n is about 0.3.

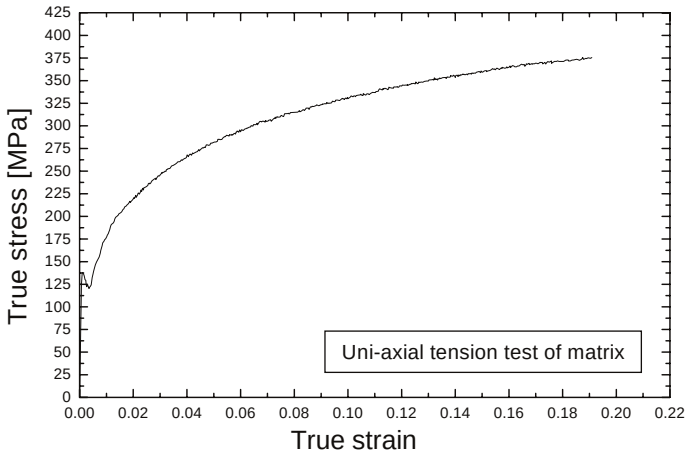

Fig. 5. The tensile true stress–strain curve of the fully dense matrix by experiment.

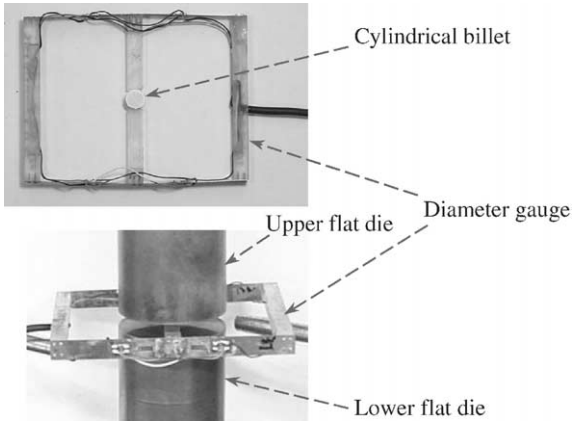

Fig. 6. The construction of the diameter gauge in the compression tests.

For the frictionless upsetting tests, the porous billets with various initial relative densities were tested under compressive loading, and Teflon sheets were used as a lubricant to maintain the uniform deformation of these specimens. Because of the compressibility of porous materials, the current cross-section of the billets during deformation cannot be determined by the relation of the incompressible volumetric plastic strain in the classical plasticity theory. Based on the assumption of the homogeneous distribution of voids in the billets, the average porosity evolution can be measured with the total change of the volume of the specimens in the frictionless upsetting. The diameter gauge, as shown in Fig. 6, was constructed to detect the current diameters of the billets during the uniform deformation, which is something imperatively needed to calculate the current area by the assumption of the circular cross-section. Therefore, the true stress in the material during the tests could be computed by dividing the current area into the axial load. On the other hand, the instantaneous heights of the billets were measured by the extensometer. Meanwhile, the void evolution was

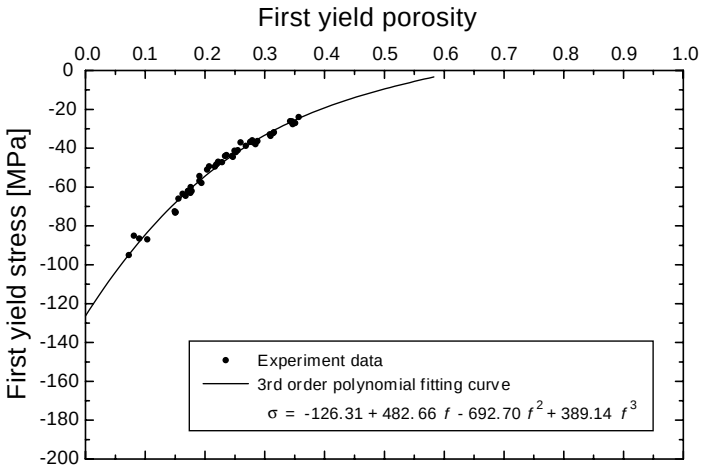

Fig. 7. Comparison of the first yield stress–porosity data by experiment and the non-linear curve by fitting.

ascertained from the total change of the volume of the billet, where the volume was calculated by multiplying the current area and the instantaneous height together.

For each frictionless upsetting test, the first yielding point is identified via the intersection of the true stress–strain curve and the line that shifted 0.2% off the elastic region. The first yield stress-porosity data, determined by upsetting the billets with various initial relative densities, are given in Fig. 7. A third order polynomial function was used to fit these data, and the empirical curve was obtained as follows:

$$\sigma_{first\ yield} = -126.31 + 482.66f - 692.70f^2 + 389.14f^3, \tag{14}$$

where $\sigma_{first\ yield}$ is the first yield stress and f is the porosity at the first yielding state. The fitting curve meets the vertical axis at -126.31 MPa, which resembles the first yield stress of the fully dense matrix in magnitude (Fig. 5). On the other hand, this curve indicates that the first yield stress approaches zero as the porosity increases to 0.62, which is close to the apparent relative density of this iron powder. The strength of the sintered materials with the densities approaching the apparent density of metal powders is insignificant.

In consideration of the Gurson–Tvergaard yield criterion, each of the material parameters contributes different effects to the plastic behaviour of porous materials. In this study, these scalar parameters were ascertained from the experiments by fitting the non-linear polynomial function, Eq. (14), into Eq. (5). The calculating loop for these parameters is presented in Fig. 2 and this program was written using the symbolic computation package Macsyma. The values of Young's modulus, E, Poisson's ratio, v, the first yield stress of the matrix, $\sigma_{first\ yield}$, and the scalar parameters of the porous metals are demonstrated in Table 2, where the parameters, q_1, q_2, and q_3, are similar to the values that Tvergaard proposed via the numerical results.

3.3. Frictional upsetting tests

Upsetting experiments without Teflon sheets were made to perform the frictional compression of porous billets, and the load–displacement curves with various initial relative densities were obtained.

Table 2
The material constants

Matrix property			Porous parameter		
E (GPa)	v	$\sigma_{first\ yield}$ (MPa)	q_1	q_2	q_3
180	0.27	126	1.81	1.00	2.80

The billets bulge out at the equatorial surface because the frictional forces inhibit the deformation of materials at contact interfaces of the billets and the flat die. The tension and compression tests were conducted using the MTS 810 material testing system, and the experiments were compared with the finite element analysis.

4. Verification of finite element analysis

4.1. Model construction

ABAQUS/Standard [34] was used to model and analyse the forging of the porous compacts. This program is developed based on the implicit code; therefore, Newton's iteration process is needed. The material properties and the deformation characteristics are very complicated in real cases, and some reasonable assumptions were made to simplify the analysis:

1. The distribution of voids is homogeneous in the specimen.
2. The matrix is perfectly bonded and incompressible.
3. The cylindrical billets are uniformly deformed in the frictionless upsetting.

The finite element mesh and the boundary conditions of the billet in the open flat die upsetting analysis are illustrated in Fig. 8. Because of the axisymmetric profile, only a quarter of each billet and die were modeled. The boundary conditions were specified on the line of symmetry. The discretization was biased toward the outward region to account for the larger amounts of deformation and the contact situations. The 8-node reduced-integration quadratic axisymmetric solid element was used for the billet, and the rigid surface was used for the flat die.

4.2. Upsetting simulation under frictionless and frictional conditions

In order to verify the finite element results with the experiments, the upsetting simulation with two different frictional conditions was considered. The coefficient of friction was given as zero in the frictionless analysis, which preserved the uniform deformation of the billets. The results were used to examine whether the inputted experimentally determined material data truly represented the actual bulk material behaviour. Then, the frictional upsetting analysis was carried out with an equivalent coefficient of friction, 0.3, which provided a similar bulged profile in loading history to the specimens from the experiments.

The compressive true stress–strain curves and the true stress–porosity curves with the initial relative densities of 0.6897, 0.8071, and 0.9058 in the frictionless upsetting are demonstrated in Figs. 9 and 10.

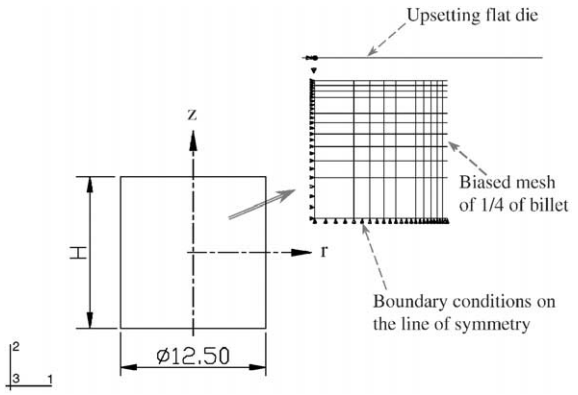

Fig. 8. The finite element mesh and the boundary conditions of the cylindrical billet in the upsetting analysis.

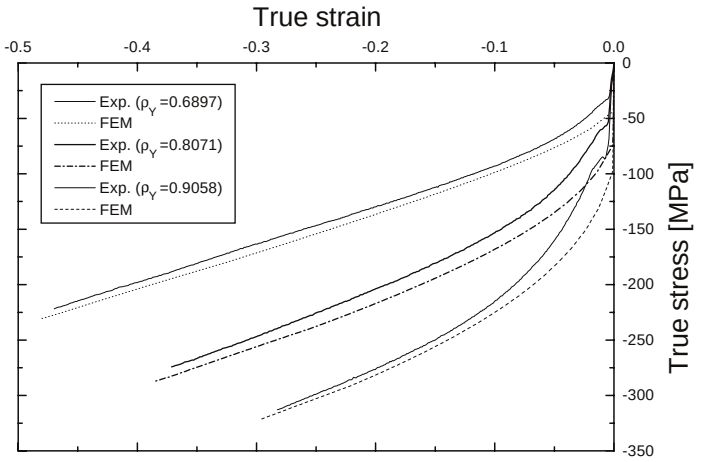

Fig. 9. Comparison of the true stress–strain curves under frictionless conditions by experiment and FEM.

The results indicate that finite element simulations closely match the measured data with slight discrepancies. Fig. 9 depicts that the yield strength and loading capacity of the workpiece deteriorate with the voids. In Fig. 10, the curves reveal the evolution of porosity during the frictionless upsetting. Void reduction is governed by the volumetric plastic strain, which is caused by the hydrostatic pressure. Errors between the finite element results and the experiments are $< 5\%$, which may have been caused by the slightly non-uniform deformation of the billets in the tests and Luders band right after the first yield that is not modeled in the finite element analysis.

From the analysis, it can be found that the material parameters in the Gurson–Tvergaard yield criterion exercise a distinct influence on the mechanical properties of porous media. The plastic behaviour of the porous materials is dominated by q_1, which deteriorates both the stress–strain and stress–porosity curves in the compressive loading. On the other hand, the parameter q_2, which weighs the effect of hydrostatic stress, bears a strong influence on the stress–porosity data. In addition, the finite element results show the insignificance of q_3.

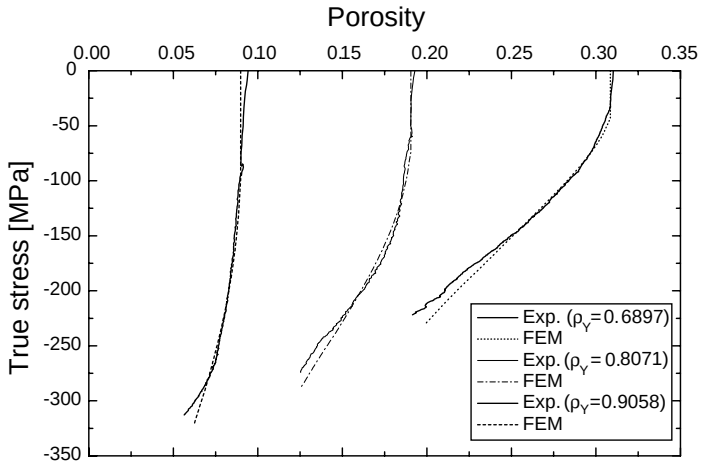

Fig. 10. Comparison of the true stress–porosity curves under frictionless conditions by experiment and FEM.

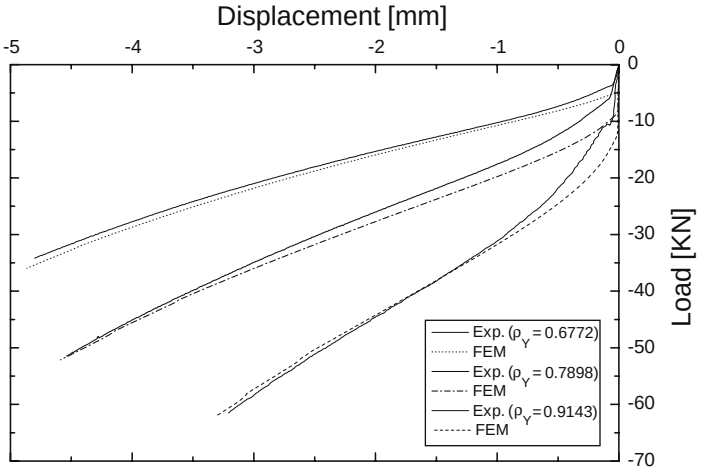

Fig. 11. Comparison of the load–displacement curves in the frictional upsetting by experiment and FEM.

As another example of validation, the same upsetting process with frictional conditions was computed. The load–displacement curves of the billets with the initial relative densities of 0.6772, 0.7898, and 0.9143 by experiment and simulation are compared in Fig. 11. Voids decrease the strength of the workpiece. Friction at contact interfaces leads to the non-uniform deformation of the workpiece, while the significant variation of the stress field is induced. The finite element results of the corresponding true stress versus true strain at the core of the billets in the frictional upsetting are demonstrated in Fig. 12. On the other hand, the contours of the relative density in the deformed workpiece are shown in Fig. 13, where the lower density exists at the equator of the bulge surface. This phenomenon is conclusively consistent with the previous investigations. Furthermore, the finite

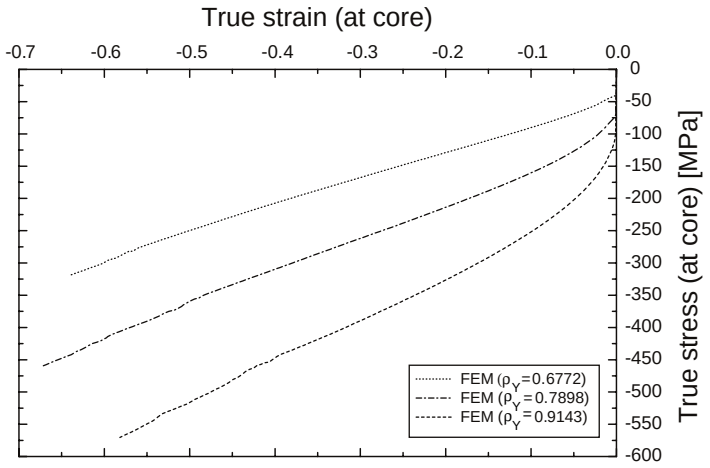

Fig. 12. The true stress–strain curves at the core of the billets in the frictional upsetting by FEM.

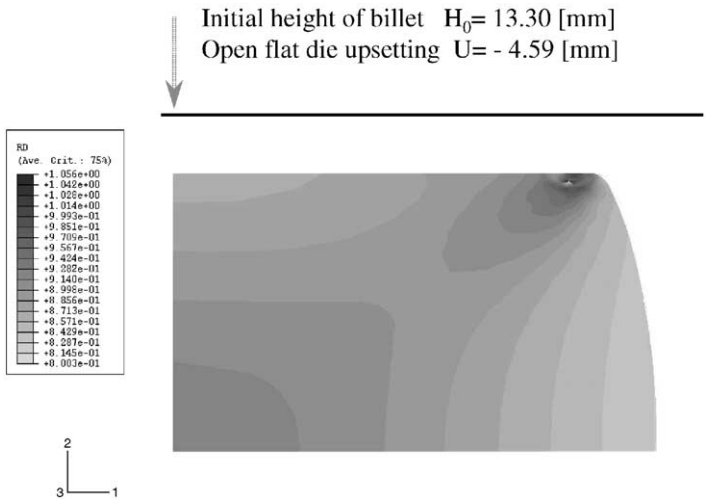

Fig. 13. The contours of the relative density in upsetting the billet under frictional conditions (coefficient of friction $\mu = 0.3$).

element models, verified with the upsetting experiments under different frictional conditions, were then applied to perform the powder forging of a gear blank.

5. Powder forging of the gear blank

5.1. Construction of the model

Bulk forming effects complicated deformation, which dominates the evolution of voids in the porous materials. In this study, we assume that the change in the void volume fraction is brought

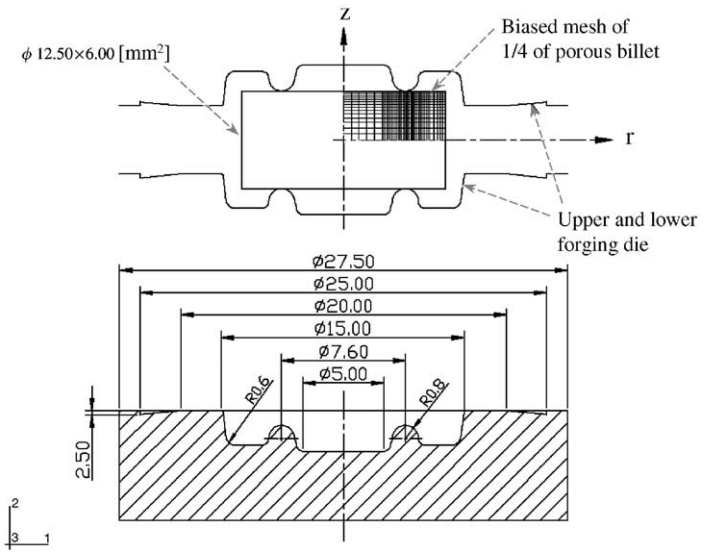

Fig. 14. The finite element mesh of the billet and the profile of the die in forging the gear blank.

about by the variation in existing voids and that the nucleation of new voids in the tensile stress is negligible.

As a practical application, powder forging of the gear blank was simulated using the results of this study to show the plastic flow characteristics of the sintered metals. The profiles of the porous billet and the forging die are illustrated in Fig. 14, where the billet is 12.5 mm in diameter and 6 mm in height, and the die is 27.5 mm in diameter. It was difficult to analyse the contact situation by using the 8-node quadratic solid element. The 4-node bilinear axisymmetric solid element, therefore, was used for the billet, and the 2-node linear axisymmetric rigid element was used to construct the die. Because of the axisymmetric profile, only a quarter of the billet and die were modeled, and the boundary conditions were also specified on the line of symmetry. The discretization was made finer in the middle region of the billet to account for the larger amounts of deformation. The material parameters in Table 2 were inputs as well.

5.2. *Forging of the gear blank under various frictional conditions*

In this analysis, the globally equivalent frictional conditions were approximated to deal with the contact situation between the workpiece and the die. In order to investigate the effects of friction on the bulk-forming process, the simulation with various frictional conditions was performed. These load–stroke curves under different coefficients of friction in forging the gear blank are demonstrated in Fig. 15.

Studies show that when the coefficient of friction used in the simulation is lower than 0.04, Newton's iteration process fails to converge. The on–off situation occurs repeatedly at the contact interfaces near the convex end of the die during the simulation. Perhaps the refined mesh in this region or the explicit code could solve this problem. On the other hand, the different coefficients of friction, which are equal to or larger than 0.04, have little effect on the load–stroke curves, while

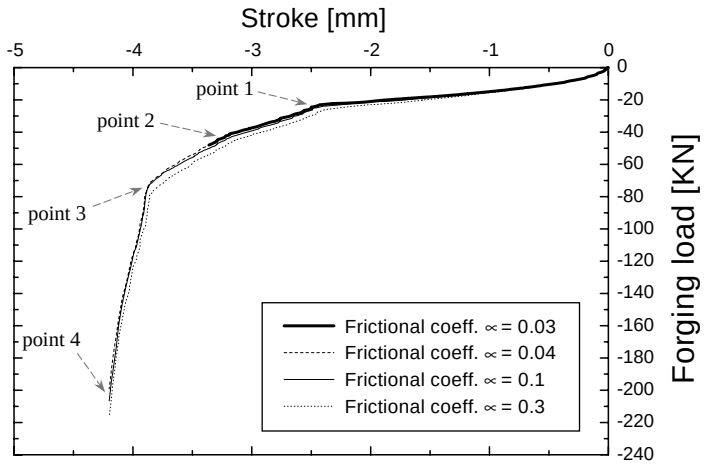

Fig. 15. The load–stroke curves in forging the gear blank under different coefficient of friction (the labels for points 1 through 4 are used in Fig. 16).

these curves almost overlap with each other. For this reason, the coefficient at a value of 0.1 was implemented into the subsequent analysis. In addition, the initial relative density of the billet was given at 0.86 for the precision forging modeling.

Moreover, the load–stroke curves in Fig. 15 also show three deflection points, which demonstrate the greatly increasing loads. In particular, the forging loads increase sharply as the die cavity is completely filled with the materials, inducing the hydrostatic pressure in the matrix. On this curve, with the coefficient of friction at 0.1, points 1–4 correspond to the strokes of 2.48, 3.15, 3.91, and 4.19 mm, respectively. The contours of the von Mises effective stress and the relative densities at those corresponding strokes are demonstrated in Fig. 16, where the contours of the effective stress are placed on the left side and the relative density variations are presented in the right column. A comparison of Figs. 15 and 16 makes it clear that every deflection point on the load–stroke curve indicates an instantaneous increase in the contact area:

Point 1 on the curve announces that the upper-right corner of the billet starts to touch the die surface, as shown in Figs. 16(1a) and (1b).

Point 2 indicates that the upper-central region starts to touch the die surface, as shown in Figs. 16(2a) and (2b). Nevertheless, the deflection at this point is not so obvious as that at points 1 and 3.

Point 3, then, indicates that the billet starts to touch the side surface of the die, as shown in Figs. 16(3a) and (3b), where the die is almost filled with the materials.

At the final stage, the die is completely filled with the materials at point 4 of the load–stroke curve in Fig. 15. It can be observed that, in Figs. 16(4a) and (4b), the effective stress distributes homogeneously and the relative density approaches the value of 1, suggesting that the voids are reduced by the hydrostatic pressure. Also, the strength of the gear blank is greatly enhanced by the forging step.

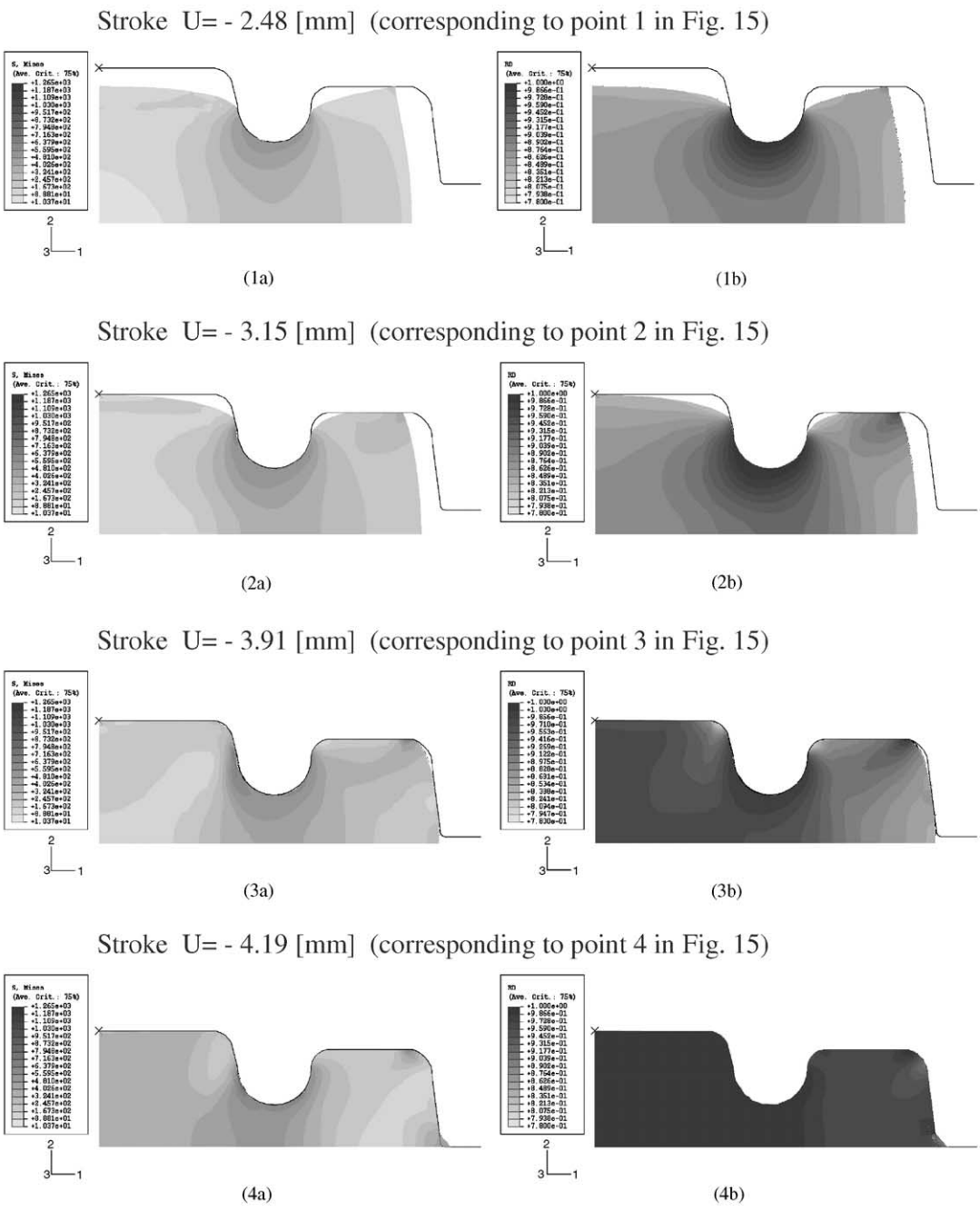

Fig. 16. The contours of the von Mises effective stress, (1a), (2a), (3a), and (4a), and the contours of the relative density, (1b), (2b), (3b), and (4b) in the deformed gear blank at various forging steps (coefficient of friction $\mu = 0.1$).

6. Conclusions

Powder forging techniques enhance the dimension precision and the strength of products. Upsetting simulation helps understand the deformation characteristics of sintered preforms. The simulation of forging the gear blank under different frictional conditions is presented as well. From the results, we draw the following conclusions:

(1) The simulation of the upsetting tests, verified with the experiments, is achieved by using the Gurson–Tvergaard yield function for porous media.
(2) The plastic behaviour of the porous metals is dominated by the parameter q_1 in the Gurson–Tvergaard criterion. The parameter q_2 bears a strong influence on the evolution of voids. In addition, q_3 is relatively insignificant.
(3) Voids lead to the degradation of the strength of the sintered materials.
(4) Friction at contact interfaces contributes to the non-uniformity of deformation and the density variation in the workpiece after large deformation.
(5) Different coefficients of friction have little effect on the forging loads during the working process.

Through the computer simulation of the forming process, we can apply the powder forging techniques with an arbitrary metal powder in complex forging applications, such as connecting rods, ratchet wheels, etc. Such capability would be helpful in optimizing the geometry of sintered preforms and forging dies. In addition, it also requires an effective fracture criterion to evaluate the forming limit of workpieces, to which we will devote ourselves in the future.

Acknowledgements

The authors acknowledge the generous support of experimental facilities from Prof. K.-S. Hwang of the Department of Materials Science and Engineering, National Taiwan University. The authors also wish to thank Prof. C.S. Shin in the NTU Department of Mechanical Engineering for providing us with the material testing system.

References

[1] Gurson AL. Continuum theory of ductile rupture by void nucleation and growth: Part I—yield criteria and flow rules for porous ductile media. Journal of Engineering Materials and Technology, Transactions of the ASME 1977; 99:2–15.
[2] Tvergaard V. Influence of voids on shear band instabilities under plane strain conditions. International Journal of Fracture 1981;17:389–407.
[3] Richmond O, Smelser RE. Alcoa Technical Center Report, 1985.
[4] Goya M, Nagaki S, Sowerby R. Yield criteria for ductile porous solids. Japan Society for Mechanical Engineering (JSME), International Journal 1992;35:310–8.
[5] Kuhn HA, Downey CL. Deformation characteristics and plasticity theory for sintered powder materials. International Journal of Powder Metallurgy 1971;7:15–25.
[6] Green RJ. A plasticity theory for porous solids. International Journal of Mechanical Sciences 1972;14:215–24.
[7] Oyane M, Shima S, Kono Y. Theory of plasticity for porous metals. Bulletin of the Japanese Society of Mechanical Engineering 1973;16:1254–62.

[8] Shima S, Oyane M. Plasticity theory for porous metals. International Journal of Mechanical Sciences 1976;18: 285–91.
[9] Doraivelu SM, Gegel HL, Gunasekera JS, Malas JC, Morgan JT. A new yield function for compressible P/M materials. International Journal of Mechanical Sciences 1984;26:527–35.
[10] Hwang BB, Kobayashi S. Deformation characterization of powdered metals in compaction. International Journal of Machining Tools and Manufacture 1990;30:309–23.
[11] Mear ME. On the plastic yielding of porous metals. Mechanics of Materials 1990;9:33–48.
[12] Lee DN, Kim HS. Plastic yield behavior of porous metals. Powder Metallurgy 1992;35:275–9.
[13] Lee BJ, Mear ME. An evaluation of Gurson's theory of dilatational plasticity. Journal of Engineering Materials and Technology, Transactions of the ASME 1993;115:339–44.
[14] Nagaki S, Goya M, Sowerby R. The influence of void distribution on the yielding of an elastic–plastic porous solid. International Journal of Plasticity 1993;9:199–211.
[15] Dias ADM, Schaeffer L. Theoretical and experimental analysis of plasticity equation for porous metals. International Journal of Machining Tools and Manufacture 1993;33:577–86.
[16] Akisanya AR, Cocks ACF, Fleck NA. The yield behaviour of metal powders. International Journal of Mechanical Sciences 1997;39:1315–24.
[17] Mear ME, Durban D. Radial flow of sintered powder metals. International Journal of Mechanical Sciences 1989;31:37–49.
[18] Bruhns O, Sluzalec A. Densification of powder metals with assumed ellipsoidal yield surface. International Journal of Mechanical Sciences 1993;35:731–40.
[19] Wang PT, Karabin ME. Evolution of porosity during thin plat rolling of powder-based porous aluminum. Powder Technology 1994;78:67–76.
[20] Han HN, Kim HS, Oh KH, Lee DN. Elastoplastic finite element analysis for porous metals. Powder Metallurgy 1994;37:140–6.
[21] Spitzig WA, Smelser RE, Richmond O. The evolution of damage and fracture in iron compacts with various initial porosity. Acta Metallurgica 1988;36:1201–11.
[22] Biner SB, Spitzig WA. Densification of iron compacts with various initial porosity under hydrostatic pressure. Acta Metallurgica et Materialia 1990;38:603–10.
[23] Spitzig WA. Effect of hydrostatic pressure on deformation, damage evolution, and fracture of iron with various initial porosity. Acta Metallurgica et Materialia 1990;38:1445–53.
[24] Hartley P, Sturgess CEN, Rowe GW. Influence of friction on the prediction of forces, pressure distributions and properties in upset forging. International Journal of Mechanical Sciences 1980;22:743–53.
[25] Jha AK, Kumar S. Deformation characteristics and fracture mechanisms during the cold forging of metal powder preforms. International Journal of Machine Tool Design & Research 1986;26:369–84.
[26] Mamalis AG, Petrossian GL, Manolakos DE. Open-die forging of sintered cylindrical billets: an analytical approach. Journal of Materials Processing Technology 1999;96:112–6.
[27] Bockstiegel G, Olsen H. Processing parameters in the hot forming of powder preforms. Powder Metallurgy, Conference Supplement, Part 1, 1971;1:127–50.
[28] Kim KT, Cho YH. Hot upsetting of porous alloy steel preforms. Powder Metallurgy 1993;36:129–34.
[29] Han HN, Lee YG, Oh KH, Lee DN. Analysis of hot forging of porous metals. Materials Science and Engineering A 1996;206:81–9.
[30] Goods SH, Brown LM. The nucleation of cavities by plastic deformation. Acta Metallurgica 1979;27:1–15.
[31] Chu CC, Needleman A. Void nucleation effects in biaxially stretched sheets. Journal of Engineering Materials Technology, Transactions of the ASME 1980;102:249–56.
[32] Hom CL, McMeeking RM. Void growth in elastic–plastic materials. Journal of Applied Mechanics, Transactions of the ASME 1989;56:309–17.
[33] Lee JH, Zhang Y. A finite-element work-hardening plasticity model of the uniaxial compression and subsequent failure of porous cylinders including effects of void nucleation and growth—Part I: plastic flow and damage. Journal of Engineering Materials and Technology, Transactions of the ASME 1994;116:69–79.
[34] Hibbit J, Karlsson, Sorensen P. ABAQUS/Standard User's Manual, Version 5.8. RI, USA: Hibbit, Karlsson & Sorensen Inc., 2000.